Translational Science

Cancer Research

Picosecond Infrared Laser Desorption Mass Spectrometry Identifies Medulloblastoma Subgroups on Intrasurgical Timescales

Michael Woolman[1,2], Claudia M. Kuzan-Fischer[3,4,5], Isabelle Ferry[3,4,5], Taira Kiyota[6], Betty Luu[3,4,5], Megan Wu[3,4,5], David G. Munoz[7], Sunit Das[3,7,8], Ahmed Aman[6], Michael D. Taylor[2,3,4,5,8], James T. Rutka[3,4,8], Howard J. Ginsberg[1,7,8,9], and Arash Zarrine-Afsar[1,2,8,9]

Abstract

Medulloblastoma (MB) is a pediatric malignant brain tumor composed of four different subgroups (WNT, SHH, Group 3, Group 4), each of which are a unique biological entity with distinct clinico-pathological, molecular, and prognostic characteristics. Although risk stratification of patients with MB based on molecular features may offer personalized therapies, conventional subgroup identification methods take too long and are unable to deliver subgroup information intraoperatively. This limitation prevents subgroup-specific adjustment of the extent or the aggressiveness of the tumor resection by the neurosurgeon. In this study, we investigated the potential of rapid tumor characterization with Picosecond infrared laser desorption mass spectrometry (PIRL-MS) for MB subgroup classification based on small molecule signatures. One hundred and thirteen *ex vivo* MB tumors from a local tissue bank were subjected to 10- to 15-second PIRL-MS data collection and principal component analysis with linear discriminant analysis (PCA-LDA). The MB subgroup model was established from 72 independent tumors; the remaining 41 de-identified unknown tumors were subjected to multiple, 10-second PIRL-MS samplings and real-time PCA-LDA analysis using the above model. The resultant 124 PIRL-MS spectra from each sampling event, after the application of a 95% PCA-LDA prediction probability threshold, yielded a 98.9% correct classification rate. Post-ablation histopathologic analysis suggested that intratumoral heterogeneity or sample damage prior to PIRL-MS sampling at the site of laser ablation was able to explain failed classifications. Therefore, upon translation, 10-seconds of PIRL-MS sampling is sufficient to allow personalized, subgroup-specific treatment of MB during surgery.

Significance: This study demonstrates that laser-extracted lipids allow immediate grading of medulloblastoma tumors into prognostically important subgroups in 10 seconds, providing medulloblastoma pathology in an actionable manner during surgery.

Introduction

Medulloblastoma (MB) is a heterogeneous posterior fossa malignancy that accounts for about 10% to 20% of all pediatric brain tumors (1–3). The heterogeneity in MB manifests itself in four known subgroups, named WNT (Wingless/iNTegrated), SHH (Sonic HedgeHog), Group 3 and Group 4 (1, 4). According to genomic analyses each MB subgroup is a distinct tumor entity that consequently carries its own molecular, as well as clinico-pathological features (5–7). MB subgroups exhibit different survival rates (6), risk of recurrence (8), and likelihood of favorable response (9) to the standard multimodal therapy comprised of maximal safe resection, chemotherapy and, for patients older than 3 years of age, cranio-spinal irradiation (10, 11). The standard risk stratification of MB patients into average and high-risk groups takes into consideration patient's age, presence of disseminated disease at diagnosis, and size of postoperative residual tumor (9).

Currently, due to the long turnaround times of the existing MB subgrouping methods of IHC and genomic analyses (12), subgroup information is not available during tumor resection. In keeping with this, the standard of care is based on the traditional risk stratification and the patient's age at the time of diagnosis and does not take into consideration MB subgroup information in planning surgical resection extents (13). All patients undergo a maximum safe resection surgery to debulk the tumor and alleviate the symptoms, followed by adjuvant chemo- and age-dependent radio-therapy (10, 14). The discovery of molecular MB subgroups,

[1]Techna Institute for the Advancement of Technology for Health, University Health Network, Toronto, Ontario, Canada. [2]Department of Medical Biophysics, University of Toronto, Ontario, Canada. [3]Peter Gilgan Centre for Research and Learning, Hospital for Sick Children, Ontario, Canada. [4]Arthur and Sonia Labatt Brain Tumor Research Centre, The Hospital for Sick Children, Toronto, Ontario, Canada. [5]Developmental & Stem Cell Biology Program, The Hospital for Sick Children, Ontario, Canada. [6]Drug Discovery Program, Ontario Institute for Cancer Research, Toronto, Ontario, Canada. [7]Keenan Research Center for Biomedical Science & the Li Ka Shing Knowledge Institute, St. Michael's Hospital, Ontario, Canada. [8]Department of Surgery, University of Toronto, Ontario, Canada. [9]Institute of Biomaterials and Biomedical Engineering, University of Toronto, Toronto, Ontario, Canada.

Note: Supplementary data for this article are available at Cancer Research Online (http://cancerres.aacrjournals.org/).

M. Woolman, C.M. Kuzan-Fischer, and I. Ferry contributed equally to this article.

Corresponding Author: Arash Zarrine-Afsar, University of Toronto, 101 College Street, Toronto, ON M5G 1L7. Phone: 4165818473; E-mail: arash.zarrine.afsar@utoronto.ca

doi: 10.1158/0008-5472.CAN-18-3411

however, has paved the way for a paradigm shift in MB subgroup specific treatment planning as evidenced by a new risk stratification method that takes into consideration the prognostic and survival information for each MB subgroup (9, 15). In this context, real-time subgrouping of MB tumors for molecularly informed clinical trials has been proposed (9). In a similar vein, a number of clinical trials (NCT02066220, NCT01878617, NCT02724579) are underway to validate de-escalation of adjuvant therapy suggested for low-risk patients with MB such as those with the nonmetastatic WNT subgroup tumors (16). The motivation behind these trials is to reduce treatment-related complications in patients with MB with favorable outcomes (9). At the moment, there is no evidence in the literature to suggest that said low-risk patients with MB above could also benefit from less aggressive surgery. The ability to determine MB subgroup information intraoperatively, however, is likely to motivate further assessments that may lead to subsequent development of subgroup specific surgical treatments in much the same way that the explorations of the validity of de-escalated adjuvant methods for low-risk patients with MB was made possible by the availability of MB subgroup information prior to adjuvant therapy planning. Recent advances in molecular classifications of MB (17–19) thus create a demand for a rapid screening tool that can resolve said molecular heterogeneities within the time constraints of surgical resection for potential future use in personalized surgery, even if those approaches cannot be envisioned in the context of the current standard of care.

Tissue small molecule profiling with a variety of ambient mass spectrometry (MS) technologies (20) such as desorption electrospray ionization (DESI-MS; refs. 21–26), rapid evaporative ionization mass spectrometry (e.g., iKnife; refs. 27, 28), SpiderMass (29), and the MasSpec pen (30) have been reported to have utility in rapid tissue identification. These techniques utilize collective changes in the lipidome and metabolome to probe molecular differences that give rise to the unique identity of each cancer type. Capitalizing on the success of these discoveries, and in the quest to deliver MB subgroup information in an actionable manner during surgery, our group has published a xenograft-based, limited feasibility assessment of a hand-held laser mass spectrometry probe that can classify Group 3 and SHH MB in only ∼5 to 10 seconds of sampling followed with post acquisition off-line data analysis (31). The probe is composed of a picosecond infrared laser (PIRL) fiber that vaporizes tumor lipid and small molecule metabolites (32) for subsequent capture and analysis by means of MS. The classification of the subcutaneous xenograft SHH and Group 3 MB tumors into their respective subclasses was achieved by comparing, using multivariate statistical methods, the PIRL-MS signatures of small molecules in unknown tumors against those of a Group 3 and SHH MB signature library (31). Our previous study provided proof-of-principle for the utility of PIRL-MS in distinguishing only Group 3 and SHH MB (31), an observation that in this manuscript is being extended to all four MB subgroups using clinical patient samples. Additionally, our previous study (31) utilized post acquisition assessments of the processed PIRL-MS spectra using off-line statistical analysis platforms, and did not allow real-time (i.e. as PIRL-MS spectra were acquired) analysis and delivery of MB subgroup classification results in a simplified manner. Real-time analysis of mass spectra poses additional technical challenges not addressed in our previous work (31) that used off-line analysis, and processed spectra. The inaccessibility of data processing techniques, such as centroid fitting, requires implementation of alternative data processing and analysis methods. Therefore, to further evaluate the translational potential of PIRL-MS as a sampling tool to reveal MB subgroup information intraoperatively within seconds, this study uses real-time multivariate analysis of PIRL-MS spectra with simplified display of the MB subgroup classification results, and provides an extension of the utility of PIRL-MS to classify all four MB subgroups using human patient samples, as opposed to xenografts. In this work we report small molecule signatures of all four MB subgroups accessed by PIRL-MS sampling, along with molecular identities of the MB subgroup classifying lipids. Our evaluation of the performance of the PIRL-MS probe in classifying MB subgroups with only 10 seconds of sampling and analysis time was performed using 113 independent banked *ex vivo* patient samples, and we demonstrate 98.9% accuracy in subgroup determination. We further report the utility of a real-time multivariate statistical analysis platform previously used for simple display of molecular pathology results such as cancer type or subtype using MS analysis of electrocautery plume (27), for MB subgroup identification with PIRL-MS. We further discuss the reproducibility, duty cycle, misclassification rate, and intra-sample performance variation metrics of the PIRL-MS platform. These insights are relevant for future adoption and potential clinical use. The overarching goal of our PIRL-MS technology development is to improve patient quality of life by making the wealth of prognostic information present within MB subgroups available to neurosurgeons such that this information can be combined with other surgical risk factors towards an efficient, personalized approach for patients with MB.

Materials and Methods

PIRL-MS data collection

A subset of 120 snap frozen MB samples gathered through Medulloblastoma Advanced Genomics International Consortium (MAGIC; ref. 33) from 30 participating centers in north America, Europe, and Asia was accessed via the Hospital for Sick Children (Toronto; ref. 17)for this study. This set thus captures some level of demographic biological variability despite its small size. The details of the sample collection and handling prior to PIRL-MS sampling are included in the Supplementary Information. These samples (∼1–6 mm^3) were obtained under Research Ethics Board approval with informed written consent; 1000057113 (Hospital for Sick Children), 17-5298 (University Health Network), 17-101 (St Michael's Hospital), and 00035377 (Ontario Institute for Cancer Research). Samples were cut on a dry ice bed, and transported on dry ice to the PIRL-MS sampling site, and thawed for ∼30 seconds before laser sampling inside a biological safety cabinet. The subgroups were known via previous NanoString assessment (34) or DNA Methylation assays, taken as "gold standard" classification (35). The description of the experimental laser setup and MS collection geometry is identical to previous work (31, 32). A PIRL operating at 1 kHz outputting ∼240 mW at 3,000 nm with pulse duration of ∼300 picoseconds was used. The PIRL fiber with a diameter of ∼0.45 mm was held 1 to 2 mm away from the surface of the *ex vivo* tissue with the tip of the ∼2 m long Tygon collection tube at close (<2 mm) proximity to the ablation site. Supplementary Fig. S1 illustrates the collection geometry of the PIRL-MS setup described previously (32), also used herein. This study did not consider any other variables

such as patient demographics, clinic of sample origin, transit or storage time, and only used subgroup information of said samples as the sole variable.

Principal component analysis-linear discriminant analysis modeling

The PIRL-MS signature models for all four MB subgroups were built using principal component analysis-linear discriminant analysis (PCA-LDA) on an "Abstract Model Builder" (AMX; version 1.0.1360.0) platform from Waters Research Centre. The PIRL-MS spectral data from Waters' MassLynx (version 4.1) software were imported directly into AMX, as recently implemented using closely related versions of this program for the classification of biological samples (36). The AMX platform offers a "model building" component where PCA-LDA analysis is used to create a multivariate model of the tissue molecular signatures, alongside a "recognition" component where blind/unknown samples can be scored against the model for classification. In this manuscript, the model was validated using blind tests. All ~15 second PIRL-MS sampling events from a given piece of tissue, contained in a single file, were then separately selected on AMX based on the rise of base peak intensity that occurred upon laser sampling where we applied a threshold of greater than 5×10^3 a.u. Additionally, samples with less than 3 seconds of persistent MS signal were excluded.

All spectral data from selected sampling events in the m/z range of 500 to 1,000 Da were put into 0.1 m/z bins and subjected to PCA-LDA analysis by AMX. The number of PCA dimensions for the model (~20% of the total number of data points in the model) was 35, with three linear dimensions. The m/z of 717.5067 ($C_{39}H_{74}O_9P$), which is represented strongly in all samples, was used to correct mass shifts (lock mass). All spectra were normalized by the total ion count (TIC). For the low complexity model we used the "peak list based PCA-LDA model" function on the AMX platform and same PCA-LDA settings as above. The mass tolerance for the peak list was set to 0.2 Da. The cross-validations via 20% leave out tests were performed using AMX with 3 × standard deviation as the boundary condition (to classify a data point as unclassifiable or outlier). The model building used ~15 second sampling events, and the classification used at most 10 seconds of sampling.

Real-time analysis of the unknown blind samples with AMX

For real-time analysis of MB subgroups we used the "AMX recognition" component, using the same lock mass and boundary conditions as above. The intensity limit was set to TIC = 2×10^5 a.u. to determine the time stamp for including an MS scan in the multivariate comparison. The "number of scans per spectrum" was set to 12 scans, and "wait for good spectrum timeout" value was 12 seconds. This meant that when the TIC rose to a value above 2×10^5 AMX started to count the MS scans until 12 seconds passed, averaging all of the spectra in this 12-second window. This average spectrum was then sent to the recognition algorithm for comparison with the uploaded PCA-LDA model and prediction of the MB subgroup of the unknown data point. The probability threshold was initially set at 0% and then increased to 90% and 95% to increase the stringency of the predictions. MB subgroup assignments from AMX were available within ~1 second after the collection of the laser plume.

Identification of MB classifying lipids from LC/MS-MS analysis of the PIRL plume

The capture and extraction of PIRL-MS laser plume was completed as described previously (31). For direct tissue extract comparisons, an 8 mm^3 piece of tissue was sliced off and carefully applied onto the filter paper, and subjected to the same extraction method as the laser plume, according to the publication above. The chromatographic separation was performed on an ACQUITY UPLC I-Class system coupled to a Waters Synapt G2-S Q-TOF-MS using conditions described in further detail in Supplementary Information.

Results

Building a statistical model for MB molecular signatures

To create a statistical model that describes MS profiles of all four MB subgroups, we subjected 75 human MB tumors (16 WNT, 20 SHH, 19 Group 3, and 20 Group 4) to ~15 seconds of PIRL-MS sampling. Inspection of the raw data (i.e., mass spectra; Supplementary Fig. S2) suggested that the PIRL-MS spectra of MB subgroups differed from one another only in terms of alterations in the abundance of small molecules, particularly in the mass to charge ratio (m/z) range of 500 to 1,000 Da. To tease out subtle changes in the small molecule abundances that could be used to identify MB subgroups, we subjected the PIRL-MS spectra (mass range of 500–1,000 Da) to a tandem of PCA-LDA. The resultant PCA-LDA model (Fig. 1A) was composed of 190 sampling events (i.e., PIRL-MS spectra or data points) collected in ~15 seconds from 15 WNT, 19 SHH, 18 Group 3, and 20 Group 4 MB (a total of 72 cancer cases from which we were able to extract good quality data upon application of exclusion criteria described in the legend of Supplementary Fig. S3). This model shows good statistical separation of the data points that belonged to each subgroup. Supplementary Table S1 summarizes the sampling period, and signal intensity values for the PIRL-MS sampling events used to build the model.

The separate grouping, in the PCA-LDA space, of the model's 190 data points based on subgroup information (Fig. 1A) attests to the specificity of PIRL-MS to identify molecular signatures specific to each MB subgroup. Fig. 1B shows the loading plots of each of the three linear dimensions of the PCA-LDA model. These plots rank the univariate m/z values (or mass spectral peaks) in terms of their contributions to the statistical discrimination between MB subgroups shown in Fig. 1A. The m/z values (on the "x" axis) are ranked (on the "y" axis) based on the extent they change intensity between subgroups, with those that lie farthest from the $y = 0$ line contributing the most. In this plot, m/z values that contribute most strongly to the statistical discrimination between MB subgroups are highlighted (see Supplementary Table S2 for the list). In Supplementary Fig. S4, we show that this limited m/z list is sufficient to statistically discriminate between all four MB subgroups.

Assessment of the robustness of the model by 20% leave out test

The robustness of the model in Fig. 1A was assessed using a 20% leave out and remodel test, where 20% of the data were iteratively excluded from the model, which was then subsequently built using the remaining 80%. The 20% "pseudo-unknowns" were then ranked for correct classification into their expected MB subgroups. The resultant misclassification rate is only interpreted to indicate robustness (the model itself is validated via blind tests

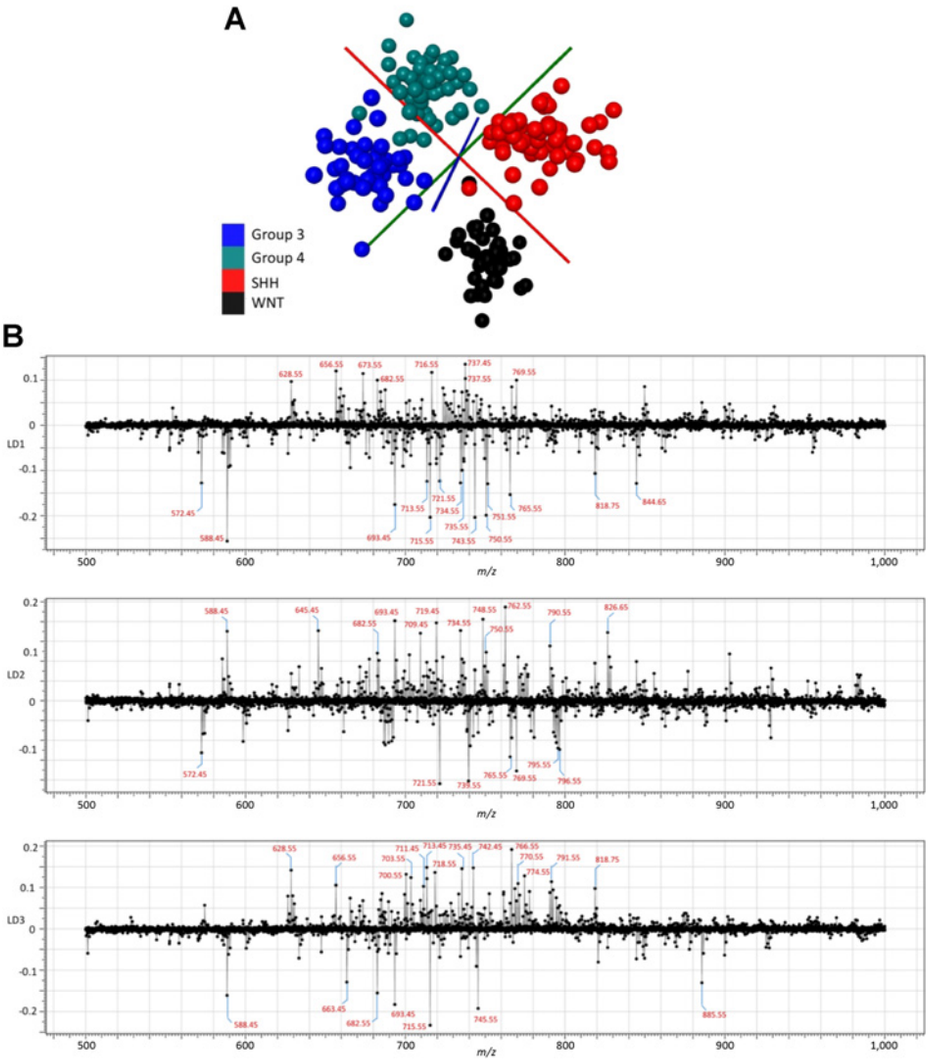

Figure 1.
The PCA-LDA model for MB subgroup differentiation using PIRL-MS analysis. The PIRL-MS spectra for MB subgroups, representatives of which are shown in Supplementary Fig. S2, were subjected to PCA-LDA analysis. The model is comprised of 190, ~15-second sampling data points from 72 independent tumor cases, with subgroup breakdowns described in the text. **A,** PCA-LDA "scores plot" illustrates statistically distinct MB subgroup signatures, suggesting that PIRL-MS spectra processed with the PCA-LDA method can tease out subtle differences in ion abundances shown in Supplementary Fig. S2 to discriminate between MB subgroups. This model was a refined version of a preliminary PCA-LDA model (shown in Supplementary Fig. S3), from which the data points that presented within or in close proximity to the data point cluster of other MB subgroups (model overlap) in the multivariate space were excluded. These data points are highlighted in Supplementary Fig. S3. According to the model overlap criterion, two additional sampling events from a Group 4 tumor were excluded. **B,** PCA-LDA "loading plots" in three linear discriminant dimensions are shown that highlight the top 44 *m/z* values that contribute the most to the statistical discrimination seen in **A**. Supplementary Table S2 provides a list of these 44 *m/z* values, which were further validated using an additional "low complexity" PCA-LDA (Supplementary Fig. S4) that only used said 44 *m/z* values. This list provided the basis for the targeted identification of MB classifying *m/z* values described in Table 3.

described below). Table 1 summarizes the results, suggesting a small 4.2% misclassification rate (8 of 190) and only 5.8% unclassifiable data points that did not classify to any of the 4 MB subgroups (11 of 190). Therefore, the model is highly robust as the majority of the data points consistently classified correctly to their respective MB subgroups. A confusion matrix is also included to indicate the breakdown, per MB subgroup, of correctly classified, unclassifiable, and misclassified data points (Table 1). As can be seen here, Group 3 and Group 4 MB showed the highest chance of misclassification. This is consistent with previous studies that have reported misclassifications between these two groups, due to genomic similarities (17).

Classifying unknown MB tumors in a blind test using the teachings of the model

To validate the model developed above, and to address potential shortcomings of the 20% leave-out-and-remodel strategy, such as redundancies in the number of biological replicates, 45

Table 1. Robustness of the PIRL-MS subgroup model from a 20% leave out test

	Data point groups					Correct classification rate	
	PIRL-MS spectra data points	Correctly classified data points	Misclassified data points	Unclassifiable data points	Classifiable data points	Per classifiable data points	Per all (classifiable and unclassifiable) data points
Total	190	171	8	11	179	95.53%	90.00%

Confusion matrix						
	Group 3	Group 4	SHH	WNT	Unclassifiable data points	Total
Group 3	39	2	1	0	3	45
Group 4	4	43	0	0	3	50
SHH	0	0	54	0	3	57
WNT	0	1	0	35	2	38
Total	43	46	55	35	11	190

NOTE: This table shows the confusion matrix for the 190 data points used to make the model described in Fig. 1A after application of an iterative 20% leave out and remodel test. A misclassification rate of 4.2% is low and suggests robustness. The test was performed using the software package Abstract Model Builder (AMX) from Waters. This matrix also illustrates the origin of misclassification into other subgroups using off-diagonal readouts. Here, the WNT data were most robust and did not misclassify, and the Group 3 and Group 4 data points presented the highest degree of misclassification into one another. Classifiable data points are defined as those data points (i.e., ∼15-second PIRL-MS spectra) that can be classified correctly or misclassified to other MB subgroups (i.e., all data points minus those that are unclassifiable to any of the MB subgroups). The correct classification rates in all of the 20% leave out and remodel tests provided in this article are reported on the basis of both (i) all data (unclassifiable and misclassified) and (ii) only classifiable data points. However, since the PIRL-MS platform is evaluable using blind samples, none of the correct classification rates from the 20% leave out tests are interpreted to indicate success. This is in keeping with concerns regarding data over fitting associated with the large number of dimensions used to tease out multivariate separations with PCA-LDA methods that require supplementing the 20% leave out test results with additional independent verifications.

de-identified MB samples not used in building of the model with subgroup breakdowns of SHH ($n = 10$), WNT ($n = 10$), Group 3 ($n = 12$), and Group 4 ($n = 13$) were subjected to 10-second sampling, and assessment against the MB subgroup model shown in Fig. 1A. The PIRL-MS operator(s) were blinded to the subgroup information during data collection and analysis. Except for four very small ($\sim$1 mm^3) WNT samples that visibly turned into liquid upon being thawed, from which we could not recover any PIRL-MS spectra, no other data points were excluded from the analysis. Supplementary Table S3 lists the prediction results for each of the resultant 124 sampling events from the 41 de-identified samples that could be analyzed. As shown here, the average sampling time of 7.4 ± 2.2 seconds corresponded to an average TIC value of $(2.6 \pm 1.3) \times 10^6$. This signal strength is comparable to the value of $(2.5 \pm 1.3) \times 10^6$ for the model itself, obtained under 14 ± 4 seconds of sampling (Supplementary Table S1), indicating reproducibility.

Table 2 provides a summary of the blind sample classification scores listed in Supplementary Table S3. Out of the total of 124 sampling events examined, 101 reported correct classifications, 7 data points were misclassified, 8 data points were of poor quality, and 8 data points were unclassifiable. Excluding the unclassifiable and poor quality data points (16 events) that could be remedied by performing additional 10-second samplings, 108 classifiable data points were generated. We report a base correct classification rate of 93.5% (101 correct assignments) over the total 108 classifiable data points. To further improve this rate, we utilized probability values available for each PCA-LDA classification (Supplementary Table S3) to re-evaluate the blind sample assessments above. Through applying various probability thresholds for PCA-LDA classification, we were able to make MB subgroup predictions of the blind samples more stringent. As illustrated in Table 2, the application of 90% and 95% thresholds increases the correct classification rate to 95.9% and 98.9% respectively, which is an improvement from the base value of 93.5% for the nonthresholded predictions. As shown in this table, the increased stringency of the prediction leads to a larger number of unclassifiable data points from 8 (nonthresholded) to 18 (90% threshold), and to 28 for the 95% probability threshold. This change is accompanied with a concomitant decrease in the number of misclassified sampling events from seven (nonthresholded) to four (90% threshold) such that at 95% probability threshold only a single sampling event is misclassified. Therefore, increasing the stringency of the predictions constitutes a good compromise to reduce the number of misclassifications.

Origin of failed classifications

To further understand the basis for the origin of failed classification events listed in Supplementary Table S3, we used post PIRL-MS pathology assessments to provide a case-by-case evaluation of the origins of misclassification and unclassifiable data points using the nonthresholded data as the basis for our comparison. Supplementary Fig. S5A–S5K provides the pathology

Table 2. Summary of blind sample classification scores

	PCA-LDA correct prediction probability threshold		
	0%	90%	95%
Data groups	PIRL-MS sampling events		
Correctly classified	101	94	87
Misclassified	7	4	1
Unclassifiable	8	18	28
Poor quality data	8	8	8
Total sampling events	124	124	124
Total classifiable sampling events	108	98	88
% correct classification (per classifiable data points)	93.50%	95.90%	98.90%

NOTE: This table summarizes the classification statistics from raw data presented in Supplementary Table S3 and also presents the results from the application of a 90% and 95% PCA-LDA prediction probability filter. As can be seen here, the increased stringency in the prediction probabilities results in an increase in the number of unclassifiable data points and a concomitant decrease in the number of misclassified samples. This leads to a desirable increase in the correct prediction rates. The correct prediction rates given are defined on the basis of the classifiable data points.

Table 3. Identification of MB subgroup classifying molecules from LC/MS-MS analysis

Target *m/z* (binned data)	PCA-LDA rank	LC/MS (*m/z*)	RT (min)	Theoretical *m/z*	Error (ppm)	Ion form	Assignment	Predicted formula	Distinguishing fragments (ms/ms)
572.45	5 (LD2)	572.4811	7.8	572.4815	0.7	$[M+Cl]^-$	Cer(d34:1)	$[C_{34}H_{67}NO_3Cl]^-$	*m/z* 237, *m/z* 280, *m/z* 308, *m/z* 506
628.55	6 (LD3)	628.5429	12.91	628.5441	1.9	$[M+Cl]^-$	Cer(d38:1)	$[C_{38}H_{75}NO_3Cl]^-$	*m/z* 293, *m/z* 336
656.55	4 (LD1)	656.5744	13.5	656.5754	1.5	$[M+Cl]^-$	Cer(d40:1)	$[C_{40}H_{79}NO_3Cl]^-$	*m/z* 237, *m/z* 321, *m/z* 364, *m/z* 380
716.55	3 (LD1)	716.5199	6.11	716.5236	5.2	$[M-CH_3]^-$	PC(32:1)	$[C_{39}H_{75}NO_8P]^-$	*m/z* 227, *m/z* 281
	-	716.5233	6.24	716.5236	0.4	$[M-CH_3]^-$	PC(32:1)	$[C_{39}H_{75}NO_8P]^-$	*m/z* 253, *m/z* 255
	-	716.5218	6.38	716.5236	2.5	$[M-CH_3]^-$	PC(32:1)	$[C_{39}H_{75}NO_8P]^-$	*m/z* 253, *m/z* 255
	-	716.5208	6.78	716.5236	3.9	$[M-CH_3]^-$	PC(32:1)	$[C_{39}H_{75}NO_8P]^-$	m/z253, *m/z* 255
742.55[a]	5 (LD3)	742.5362	6.48	742.5392	4	$[M-CH_3]^-$	PC(34:2)	$[C_{41}H_{77}NO_8P]^-$	*m/z* 253, *m/z* 281
742.55[a]	5 (LD3)	742.5362	6.48	742.5392	4	$[M-CH_3]^-$	PC(34:2)	$[C_{41}H_{77}NO_8P]^-$	*m/z* 255, *m/z* 279
748.55	3 (LD2)	748.5267	7.43	748.5287	2.7	[M-H]-	PE(P-38:5)	$[C_{43}H_{75}NO_7P]^-$	*m/z* 303, *m/z* 444, *m/z* 462
750.55	2 (LD1)	750.543	8.99	750.5443	1.7	$[M-H]^-$	PE(P-38:4)	$[C_{43}H_{77}NO_7P]^-$	*m/z* 331, *m/z* 436
	-	750.5414	9.68	750.5443	3.9	$[M-H]^-$	PE(P-38:4)	$[C_{43}H_{77}NO_7P]^-$	*m/z* 303, *m/z* 446, *m/z* 464
766.55	2 (LD3)	766.5352	6.28	766.5392	5.2	$[M-CH_3]^-$	PC(36:4)	$[C_{43}H_{77}NO_8P]^-$	*m/z* 255, *m/z* 303
	-	766.5372	8.59	766.5392	2.6	$[M-H]^-$	PE(38:4)	$[C_{43}H_{77}NO_8P]^-$	*m/z* 283, *m/z* 303
774.55	7 (LD3)	774.5424	8.92	774.5443	2.5	$[M-H]^-$	PE(P-40:6)	$[C_{45}H_{77}NO_7P]^-$	*m/z* 327, *m/z* 446, *m/z* 464
885.55	7 (LD3)	885.546	6.7	885.5499	4.4	$[M-H]^-$	PI(38:4)	$[C_{47}H_{82}O_{13}P]^-$	*m/z* 283, *m/z* 303

NOTE: This table lists the target mass (from binned PIRL-MS data, 0.1 *m/z*, on a Xevo q-ToF), accurate mass (from LC/MS on high-resolution Synapt), retention times (from LC) as well as mass shift (error ppm) from comparison of the experimental and theoretical mass [LipidMaps(37)], ion form, fragmentation pattern from MS-MS as well as rank order by which each identified molecule contributes to the PCA-LDA discrimination of MB subgroups. All identified molecules contribute strongly to discrimination of MB subgroups as shown by the indicated rank order in each linear dimension (Fig. 1B). We have also shown distinguishing fragments from MS-MS analysis used to provide lipid chain assignments. Predicted chemical formulas were determined based on accurate mass, elemental composition analysis (MassLynx) and LipidMaps database search. Representative PIRL-MS spectra from q-TOF were subjected to lock mass correction and used as a guide to determine corresponding LC/MS *m/z* values from Synapt.

[a]Two isobaric lipids were co-eluted.

annotations for all sampling events that were misclassified or were unclassifiable using the PIRL-MS model of MB subgroups (Fig. 1A). As illustrated in the legend that accompanies Supplementary Fig. S5, the aberrantly high ratios of stroma that localized to the sampling sites as well as infiltration of healthy brain tissue, likely not accounted for in the MB subgroup model used, can explain the origin of most misclassifications and many of the unclassifiable data points. Although the demonstrated hypersensitivity of PIRL-MS to molecular heterogeneity at the sampling sites attests to its superb specificity, more extensive PIRL-MS models that take signatures of stroma as well as healthy brain tissue into consideration may be required to reduce the number of failed classifications.

To further show the correlation between hypersensitive extractions of MB classifying signatures and tissue morphology at the sampled regions, in Supplementary Fig. S6A we examined the statistical similarity between the PIRL-MS profiles of misclassified/unclassifiable data points and those that correctly classified into their respective MB subgroups. Here, we used PCA-LDA score plots to compare the PIRL-MS profiles of these two data groups. As illustrated here, the misclassified and unclassifiable data points possessed distinct PIRL-MS profiles compared with correctly classified data points with heavily damaged sample 1266, stroma-rich samples 2636 and 2100, as well as healthy brain tissue containing sample 2378 being most statistically different from the correctly classified data points (Supplementary Fig. S5). Here, the data points that lie too close to the multivariate space populated with correctly classified data points may misclassify, and those that are most dissimilar will remain unclassifiable. In keeping with this observation, the application of the 95% probability threshold to make the predictions more stringent is shown to eliminate all but one of the misclassified data points (Table 2). In the absence of more extensive models inclusive of a broader range of heterogeneity signatures suggested above, thresholding predictions seems effective to mitigate misclassifications in MB. Here, we speculate that the concomitant increase in the number of unclassifiable data points that arise as a consequence of enhancing the stringency of the predictions may be remedied by performing additional 5 to 10 second samplings. To validate the clustering of the misclassified/unclassifiable data points and the correctly classified ones in Supplementary Fig. S6A, we also created a four-member PCA-LDA model that possessed randomly scrambled spectra from each MB subgroup. The randomly grouped MB data points (Supplementary Fig. S6B) show no statistical discrimination once subjected to PCA-LDA assessment. Therefore, the separation seen in Supplementary Fig. S6A, indicative of the role of tumor heterogeneity in model failure, is a valid observation. In addition, lack of statistical grouping of randomized data in Supplementary Fig. S6B also suggests significant overfitting of the PIRL-MS data by AMX is unlikely to be taking place in other multivariate examinations presented in this work.

Identification of MB classifying molecules with plume capture and high-resolution MS analysis

To determine the molecular identities of the MB subgroup classifying lipids through a targeted approach, we captured the plume of the PIRL desorption on a filter paper using a representative Group 4 MB tumor (sample ID 1365) that contained all of the 44 *m/z* values identified above to drive MB subgroup separation (Fig. 1B; Supplementary Table S2). The filter paper containing the laser extracted tissue molecules was then subjected to chemical extraction of lipids followed by analysis with high-resolution MS after LC using protocols developed and published previously (31). We also performed MS-MS analysis to further narrow down the lipid chain assignments using known lipid fragmentation patterns (37). To demonstrate that the PIRL desorption is capable of extracting tissue molecular content in a state that is not drastically different from conventional methods

of molecular extraction for MS analysis, we compared the LC elution profiles of the laser plume (used in PIRL-MS to differentiate tissues) to that of the non-laser sampled tissue (used in conventional lipid MS studies), both subjected to identical chemical extraction conditions for LC. As shown in Supplementary Fig. S7, the same species dominated both elution profiles. This close match indicates that the proposed LC/MS method is a valid tool to identify MB classifying molecules as the PIRL-MS differentiation of MB subgroups appears to be based on biologically relevant molecules. Table 3 summarizes the lipid assignments for 10 molecules robustly identified via targeted analysis that contribute to MB subgroup classification. These molecules are shown to strongly contribute to PCA-LDA separation (rank orders within top 10 in each linear dimension). As seen here, the differentiation is based on a variety of lipid classes such as ceramides, phosphatidylethanolamines and phosphatidylcholines.

Discussion

Here, we provide evidence that, upon translation, PIRL-MS technology with its hand-held sampling probe will provide intraoperative MB subgrouping. This information could now influence the extent of resection and hence patient outcomes through predicting risk of relapse and likelihood of favorable response to adjuvant therapy. The utility of the model developed here using frozen tissue for real-time analysis of fresh surgical specimens is to be evaluated. However, to further assess the potential for clinical utility we also undertook an analysis of previously frozen surgical specimens sampled with PIRL-MS for a measure of concordance for spatially invariant MB subgroup assignment results. As illustrated in Supplementary Information, an average intrasample spatially invariant assignment rate of upwards of 90% is possible with PIRL-MS, where the results of the subgroup determinations do not depend on the location of the sampled site on the surface of the tumor. The high confidence seen for spatially invariant sampling results is an important practical attribute that makes PIRL-MS analysis robust in the context of spatially varying sites of biopsy. In much the same way that the full impact of genomic identification of MB subgroups as a risk stratification tool described above (9) was not necessarily envisioned at inception, we are unable to provide literature evidence as to how the ability to determine MB subgroups on intrasurgical timescales can be leveraged to provide personalized surgical treatments to patients with MB in the current standard of care. However, we are able to highlight a number of possibilities. For example, where the risk of neurologic morbidity is high and MB subgroup information suggests a good response to adjuvant therapy and a low chance for relapse, the surgeon may choose a less aggressive approach to resection. Likewise, in the case of MB patients belonging to tumor subgroups with poor prognosis, for example metastatic Group 4 patients, who do not seem to benefit from extensive resection due to the extensive leptomeningeal dissemination, the surgeon may choose a less aggressive approach to favor quality of life (38). In a similar vein, MB patients with incomplete initial resection have been traditionally regarded as high risk (>1.5 cm^2 of residual tumor present after surgery), and have been subjected to adjuvant chemotherapy and high-dose radiotherapy (if >3 years of age; ref. 38). Therefore, low-risk patients with a survival >90% such as nonmetastatic WNT patients based on the molecular risk stratification (9) potentially benefit from less aggressive surgery, especially if the possibility of significant neurologic morbidity due to aggressive resection in the posterior fossa is considered to be high. The availability of subgroup information during surgery may be crucial in these cases, as it could allow the neurosurgeon to adjust the extent of tumor resection according to the most favorable subgroup-based outcome information.

This work additionally highlights the utility of small molecule tissue profiling with PIRL-MS in tumor classification as a complementary tool to transcriptomic or genomic approaches currently in use for tumor subgroup identification, and further tumor subtype classifications. Although the lipidome and metabolome lack a one-to-one correspondence to the genome, our technique adds to the plethora of rapid ambient mass spectrometric methods of metabolomic profiling reported to classify tumor types in a manner consistent with genetic profiling (20). To better rationalize the involvement of the classes of lipid summarized in Table 3 in MB pathology, a future untargeted study aimed at elucidating all MB classifying lipids identifiable with MS is required. A deeper understanding of the lipid pathways may help explain the utility of PIRL-MS in MB classification. With this caveat, this study nevertheless adds to the growing list of ambient MS technologies that use lipid signatures to characterize cancer (22–26, 39, 40), and forms the basis of a new method to classify MB with the unparalleled advantage of speed without sacrificing specificity. Capitalizing on the significant alterations of the lipidome during oncogenesis (41), a myriad of mass spectrometry technologies have already used lipid signatures to classify cancerous tissues (39). Metabolic reprogramming in cancer cells is empirically shown to also have utility in further cancer classification into clinically relevant types and subtypes with MS (22–26, 39, 40). Currently, RNA expression profiling using NanoString methods utilizing the expression levels of only 22 MB subgroup specific signature genes (34) have been shown robust and promising to classify MB. In a similar vein, DNA methylation profiles have been shown to have utility in central nervous system tumor classification (42), including MB (43), offering advantages over NanoString (35). Further incorporation of genome-wide DNA methylation profiles has also been used to reveal additional MB subtypes (17). Although there is knowledge about the genes enriched in each MB subgroup (17), the link between the gene list empirically shown to have utility in NanoString classification, those significant in methylation profiling and the lipids identified herein with PIRL-MS requires additional work to make apparent. Nevertheless, a cursory examination of the reporter genes used in NanoString (35) indicates involvement of a variety of enzymes such as glutamate decarboxylase, glyceroaldehyde-3-phosphate dehydrogenase, and lactate dehydrogenase that play direct roles in small molecule metabolism. Therefore, it may not be entirely surprising that the PIRL-MS analysis of the tissue small molecules provides the same classification results as the genomic assays, albeit using a different set of molecular observables. Whether metabolic nuances provide sufficient contrast to capture grading of MB subgroups into additional subtypes (17) remains to be evaluated. In this quest, other non-ambient mass spectrometric analysis methods such as Matrix Assisted Laser Desorption Ionization Mass Spectrometry (MALDI-MS) can also be useful (44–49). Similar to many other rapid mass spectrometry classification methods reviewed above [iKnife (28), SpiderMass (29), MasSpec Pen (30)], PIRL-MS is likely to find utility

for *ex vivo* and *in situ*/*in vivo* tissue examination scenario (Supplementary Fig. S8) where its limited thermal and mechanical damage to regions outside the ablation zone (50) will be leveraged in adoption.

Disclosure of Potential Conflicts of Interest

No potential conflicts of interest were disclosed.

Authors' Contributions

Conception and design: T. Kiyota, A. Aman, H.J. Ginsberg, A. Zarrine-Afsar
Development of methodology: M. Woolman, C.M. Kuzan-Fischer, I. Ferry, T. Kiyota, A. Aman, H.J. Ginsberg, A. Zarrine-Afsar
Acquisition of data (provided animals, acquired and managed patients, provided facilities, etc.): M. Woolman, C.M. Kuzan-Fischer, I. Ferry, T. Kiyota, D.G. Munoz, S. Das, A. Aman, M.D. Taylor, A. Zarrine-Afsar
Analysis and interpretation of data (e.g., statistical analysis, biostatistics, computational analysis): M. Woolman, C.M. Kuzan-Fischer, T. Kiyota, M. Wu, D.G. Munoz, A. Aman, A. Zarrine-Afsar
Writing, review, and/or revision of the manuscript: M. Woolman, C.M. Kuzan-Fischer, I. Ferry, T. Kiyota, M. Wu, D.G. Munoz, S. Das, A. Aman, J.T. Rutka, H.J. Ginsberg, A. Zarrine-Afsar
Administrative, technical, or material support (i.e., reporting or organizing data, constructing databases): I. Ferry, B. Luu
Study supervision: A. Zarrine-Afsar

Acknowledgments

We are grateful to Craig Daniels, Jim Loukides (Hospital for Sick Children), Jeff O'Meara (Ontario Institute for Cancer Research), and Ori Rotstein (St. Michael's Hospital) for assistance and advice. Authors thank Stacey Krumholtz, Medical Illustrator at The Hospital for Sick Children, Toronto, Canada, for preparation of setup schematics. This work received Foundation support from Princess Margaret Hospital (to A. Zarrine-Afsar) and St. Michael's Hospital (to A. Zarrine-Afsar and H.J. Ginsberg). A. Zarrine-Afsar further acknowledges support from Natural Sciences and Engineering Research Council of Canada Discovery Grant Program (NSERC, RGPIN-2018-04611) for PIRL-MS platform development. Authors additionally thank STTARR Innovation Centre (www.sttarr.com) and its affiliated funders.

The costs of publication of this article were defrayed in part by the payment of page charges. This article must therefore be hereby marked *advertisement* in accordance with 18 U.S.C. Section 1734 solely to indicate this fact.

Received October 31, 2018; revised February 13, 2019; accepted March 14, 2019; published first March 19, 2019.

References

1. Northcott PA, Korshunov A, Witt H, Hielscher T, Eberhart CG, Mack S, et al. Medulloblastoma comprises four distinct molecular variants. J Clin Oncol 2011;29:1408–14.
2. Ostrom QT, Gittleman H, Fulop J, Liu M, Blanda R, Kromer C, et al. CBTRUS statistical report: primary brain and central nervous system tumors diagnosed in the United States in 2008–2012. Neuro Oncol 2015;17:iv1–iv62.
3. Ostrom QT, de Blank PM, Kruchko C, Petersen CM, Liao P, Finlay JL, et al. Alex's lemonade stand foundation infant and childhood primary brain and central nervous system tumors diagnosed in the United States in 2007–2011. Neuro Oncol 2015;16:x1–x36.
4. Taylor MD, Northcott PA, Korshunov A, Remke M, Cho YJ, Clifford SC, et al. Molecular subgroups of medulloblastoma: the current consensus. Acta Neuropathol 2012;123:465–72.
5. Kool M, Koster J, Bunt J, Hasselt NE, Lakeman A, van Sluis P, et al. Integrated genomics identifies five medulloblastoma subtypes with distinct genetic profiles, pathway signatures and clinicopathological features. PLoS One 2008;3:e3088.
6. Kool M, Korshunov A, Remke M, Jones DT, Schlanstein M, Northcott PA, et al. Molecular subgroups of medulloblastoma: an international meta-analysis of transcriptome, genetic aberrations, and clinical data of WNT, SHH, Group 3, and Group 4 medulloblastomas. Acta Neuropathol 2012;123:473–84.
7. Jones DT, Jager N, Kool M, Zichner T, Hutter B, Sultan M, et al. Dissecting the genomic complexity underlying medulloblastoma. Nature 2012;488:100–5.
8. Ramaswamy V, Remke M, Bouffet E, Faria CC, Perreault S, Cho YJ, et al. Recurrence patterns across medulloblastoma subgroups: an integrated clinical and molecular analysis. Lancet Oncol 2013;14:1200–7.
9. Ramaswamy V, Remke M, Bouffet E, Bailey S, Clifford SC, Doz F, et al. Risk stratification of childhood medulloblastoma in the molecular era: the current consensus. Acta Neuropathol 2016;131:821–31.
10. Gajjar AJ, Robinson GW.Medulloblastoma-translating discoveries from the bench to the bedside. Nat Rev Clin Oncol 2014;11:714–22.
11. Massimino M, Biassoni V, Gandola L, Garre ML, Gatta G, Giangaspero F, et al. Childhood medulloblastoma. Crit Rev Oncol Hematol 2016;105:35–51.
12. Gottardo NG, Hansford JR, McGlade JP, Alvaro F, Ashley DM, Bailey S, et al. Medulloblastoma Down Under 2013: a report from the third annual meeting of the International Medulloblastoma Working Group. Acta Neuropathol (Berl) 2014;127:189–201.
13. Ramaswamy V, Taylor MD. Medulloblastoma: from myth to molecular. J Clin Oncol 2017;35:2355–63.
14. Ramaswamy V, Remke M, Adamski J, Bartels U, Tabori U, Wang X, et al. Medulloblastoma subgroup-specific outcomes in irradiated children: who are the true high-risk patients? Neuro Oncol 2016;18:291–7.
15. Gajjar A, Pfister SM, Taylor MD, Gilbertson RJ. Molecular insights into pediatric brain tumors have the potential to transform therapy. Clin Cancer Res 2014;20:5630–40.
16. Holgado BL, Stucklin AG, Garzia L, Daniels C, Taylor MD. Tailoring medulloblastoma treatment through genomics: making a change, one subgroup at a time. Annu Rev Genom Hum G 2017;18:143–66.
17. Cavalli FMG, Remke M, Rampasek L, Peacock J, Shih DJH, Luu B, et al. Intertumoral heterogeneity within medulloblastoma subgroups. Cancer Cell 2017;31:737–54 e6.
18. Northcott PA, Buchhalter I, Morrissy AS, Hovestadt V, Weischenfeldt J, Ehrenberger T, et al. The whole-genome landscape of medulloblastoma subtypes. Nature 2017;547:311–7.
19. Schwalbe EC, Lindsey JC, Nakjang S, Crosier S, Smith AJ, Hicks D, et al. Novel molecular subgroups for clinical classification and outcome prediction in childhood medulloblastoma: a cohort study. Lancet Oncol 2017;18:958–71.
20. Takats Z, Strittmatter N, McKenzie JS. Ambient mass spectrometry in cancer research. Adv Cancer Res 2017;134:231–56.
21. Wiseman JM, Ifa DR, Song Q, Cooks RG. Tissue imaging at atmospheric pressure using desorption electrospray ionization (DESI) mass spectrometry. Angew Chem Int Ed Engl 2006;45:7188–92.
22. Eberlin LS, Norton I, Orringer D, Dunn IF, Liu X, Ide JL, et al. Ambient mass spectrometry for the intraoperative molecular diagnosis of human brain tumors. Proc Natl Acad Sci U S A 2013;110:1611–6.
23. Eberlin LS, Norton I, Dill AL, Golby AJ, Ligon KL, Santagata S, et al. Classifying human brain tumors by lipid imaging with mass spectrometry. Cancer Res 2012;72:645–54.
24. Eberlin LS, Dill AL, Golby AJ, Ligon KL, Wiseman JM, Cooks RG, et al. Discrimination of human astrocytoma subtypes by lipid analysis using desorption electrospray ionization imaging mass spectrometry. Angew Chem Int Ed Engl 2010;49:5953–6.
25. Eberlin LS, Tibshirani RJ, Zhang J, Longacre TA, Berry GJ, Bingham DB, et al. Molecular assessment of surgical-resection margins of gastric cancer by mass-spectrometric imaging. Proc Natl Acad Sci U S A 2014;111:2436–41.
26. Eberlin LS, Gabay M, Fan AC, Gouw AM, Tibshirani RJ, Felsher DW, et al. Alteration of the lipid profile in lymphomas induced by MYC overexpression. Proc Natl Acad Sci U S A 2014;111:10450–5.
27. Balog J, Szaniszlo T, Schaefer KC, Denes J, Lopata A, Godorhazy L, et al. Identification of biological tissues by rapid evaporative ionization mass spectrometry. Anal Chem 2010;82:7343–50.

28. Balog J, Sasi-Szabo L, Kinross J, Lewis MR, Muirhead LJ, Veselkov K, et al. Intraoperative tissue identification using rapid evaporative ionization mass spectrometry. Sci Transl Med 2013;5:194ra93.
29. Fatou B, Saudemont P, Leblanc E, Vinatier D, Mesdag V, Wisztorski M, et al. In vivo real-time mass spectrometry for guided surgery application. Sci Rep 2016;6:25919.
30. Zhang J, Rector J, Lin JQ, Young JH, Sans M, Katta N, et al. Nondestructive tissue analysis for ex vivo and in vivo cancer diagnosis using a handheld mass spectrometry system. Sci Transl Med 2017;9. doi: 10.1126/scitranslmed.aan3968.
31. Woolman M, Ferry I, Kuzan-Fischer CM, Wu MG, Zou J, Kiyota T, et al. Rapid determination of medulloblastoma subgroup affiliation with mass spectrometry using a handheld picosecond infrared laser desorption probe. Chem Sci 2017;8:6508–19.
32. Woolman M, Gribble A, Bluemke E, Zou J, Ventura M, Bernards N, et al. Optimized mass spectrometry analysis workflow with polarimetric guidance for ex vivo and in situ sampling of biological tissues. Sci Rep 2017;7:468. doi: 10.1038/s41598-017-00272-y.
33. Northcott PA, Shih DJ, Peacock J, Garzia L, Morrissy AS, Zichner T, et al. Subgroup-specific structural variation across 1,000 medulloblastoma genomes. Nature 2012;488:49–56.
34. Northcott PA, Shih DJ, Remke M, Cho YJ, Kool M, Hawkins C, et al. Rapid, reliable, and reproducible molecular sub-grouping of clinical medulloblastoma samples. Acta Neuropathol 2012;123:615–26.
35. Korshunov A, Chavez L, Northcott PA, Sharma T, Ryzhova M, Jones DTW, et al. DNA-methylation profiling discloses significant advantages over NanoString method for molecular classification of medulloblastoma. Acta Neuropathol 2017;134:965–7.
36. Bodai Z, Cameron S, Bolt F, Simon D, Schaffer R, Karancsi T, et al. Effect of electrode geometry on the classification performance of rapid evaporative ionization mass spectrometric (REIMS) bacterial identification. J Am Soc Mass Spectrom 2018;29:26–33.
37. Fahy E, Sud M, Cotter D, Subramaniam S. LIPID MAPS online tools for lipid research. Nucleic Acids Res 2007;35:W606–12.
38. Thompson EM, Hielscher T, Bouffet E, Remke M, Luu B, Gururangan S, et al. Prognostic value of medulloblastoma extent of resection after accounting for molecular subgroup: a retrospective integrated clinical and molecular analysis. Lancet Oncol 2016;17:484–95.
39. Ifa DR, Eberlin LS.Ambient ionization mass spectrometry for cancer diagnosis and surgical margin evaluation. Clin Chem 2016;62:111–23.
40. Calligaris D, Caragacianu D, Liu X, Norton I, Thompson CJ, Richardson AL, et al. Application of desorption electrospray ionization mass spectrometry imaging in breast cancer margin analysis. PNAS 2014;111:15184–9.
41. Santos CR, Schulze A. Lipid metabolism in cancer. FEBS J 2012;279:2610–23.
42. Capper D, Jones DTW, Sill M, Hovestadt V, Schrimpf D, Sturm D, et al. DNA methylation-based classification of central nervous system tumours. Nature 2018;555:469–74.
43. Hovestadt V, Remke M, Kool M, Pietsch T, Northcott PA, Fischer R, et al. Robust molecular subgrouping and copy-number profiling of medulloblastoma from small amounts of archival tumour material using high-density DNA methylation arrays. Acta Neuropathol 2013;125:913–6.
44. Bestard-Escalas J, Garate J, Maimo-Barcelo A, Fernandez R, Lopez DH, Lage S, et al. Lipid fingerprint image accurately conveys human colon cell pathophysiologic state: a solid candidate as biomarker. Biochim Biophys Acta 2016;1861:1942–50.
45. Mascini NE, Teunissen J, Noorlag R, Willems SM, Heeren RMA. Tumor classification with MALDI-MSI data of tissue microarrays: a case study. Methods 2018;151:21–7.
46. Herring KD, Oppenheimer SR, Caprioli RM. Direct tissue analysis by matrix-assisted laser desorption ionization mass spectrometry: application to kidney biology. Semin Nephrol 2007;27:597–608.
47. Ly A, Buck A, Balluff B, Sun N, Gorzolka K, Feuchtinger A, et al. High-mass-resolution MALDI mass spectrometry imaging of metabolites from formalin-fixed paraffin-embedded tissue. Nat Protoc 2016;11:1428–43.
48. Dilillo M, Ait-Belkacem R, Esteve C, Pellegrini D, Nicolardi S, Costa M, et al. Ultra-high mass resolution MALDI imaging mass spectrometry of proteins and metabolites in a mouse model of glioblastoma. Sci Rep 2017;7:603. doi: 10.1038/s41598-017-00703-w.
49. Balluff B, McDonnell LA.Mass Spectrometry Imaging of Metabolites. Methods Mol Biol 2018;1730:345–57.
50. Amini-Nik S, Kraemer D, Cowan ML, Gunaratne K, Nadesan P, Alman BA, et al. Ultrafast mid-IR laser scalpel: protein signals of the fundamental limits to minimally invasive surgery. PLoS One 2010;5. doi: 10.1371/journal.pone.0013053.